The Formation of a High Pressure Staircase Pedestal with Suppressed Edge-Localized-Modes in the DIII-D Tokamak

Arash Ashourvan[1], R. Nazikian[1], E. Belli[2], J. Candy[2], D. Eldon[2], B.A. Grierson[1], W. Guttenfelder[1], S.R. Haskey[1], C. Lasnier[3], G.R. McKee[4], and C.C. Petty[2]
[1]*Princeton Plasma Physics Laboratory, Princeton, New Jersey 08540, USA*
[2]*General Atomics, PO Box 85608, San Diego, CA 92186-5608, USA*
[3]*Lawrence Livermore National Laboratory, 7000 East Ave, Livermore, CA 94550, USA*
[4]*University of Wisconsin-Madison, 1500 Engineering Dr., Madison, WI 53706, USA*

We observe the formation of a high-pressure staircase pedestal ($\approx$ 16 - 20 kPa) in the DIII-D tokamak when large amplitude Edge-Localized-Modes are suppressed using resonant magnetic perturbations. The staircase pedestal is characterized by a flattening of the density and temperature profiles in mid-pedestal creating a two-step staircase pedestal structure correlated with the appearance of mid-pedestal broadband fluctuations. The pedestal oscillates between the staircase and single-step structure every 40-60 ms, correlated with oscillations in the heat and particle flux to the divertor. Gyrokinetic analysis using the CGYRO code shows that when the heat and particle flux to the divertor decreases, the pedestal broadens and the E×B shear at the mid-pedestal decreases, triggering a transport bifurcation from Kinetic-Ballooning-Mode (KBM) to Trapped-Electron-Mode (TEM) limited transport that flattens the density and temperature profiles at mid-pedestal and results in the formation of the staircase pedestal. As the heat flux to the divertor increases, the pedestal narrows and the E×B shear at the mid-pedestal increases, triggering a back transition from TEM to KBM limited transport. The pedestal pressure increases during the staircase phase, indicating that enhanced mid-pedestal turbulence can be beneficial for confinement.

A historic advance in magnetic fusion research was the discovery of H-mode confinement [1] resulting from the formation of an edge transport barrier. The standard paradigm for the H-mode transition is the formation of an edge transport barrier when the E×B velocity shear is sufficient to suppress long wavelength instabilities [2]. More recently it has been shown that the dual constraint of Peeling-Ballooning-Mode (PBM) and Kinetic-Ballooning-Mode (KBM) stability captures key features of the edge transport barrier including the height and width of the pedestal [3]. However, new theoretical studies [4, 5] suggest that the KBM may not always be the limiting instability in the gradient region of the pedestal, and that as we move to reactor scale with smaller $\rho^* = \rho_s/a$ (ρ_s ion sound radius, a minor radius), the E×B shear may be insufficient to suppress long wavelength instabilities in the pedestal, with potentially deleterious effects on H-mode confinement [4].

In a recent study it has been shown that n=3 Resonant Magnetic Perturbations (RMPs) suppress large amplitude edge-localized-modes (ELMs) in DIII-D high β_p ($\beta_p > 1.5$) plasmas leaving residual high frequency ELMs known as "grassy"-ELMs in a naturally wide pedestal regime [6]. These plasmas typically have double the edge pressure and pedestal width of ITER baseline plasmas with similar shape, toroidal field, and total stored energy ($\approx$1 MJ) [6, 7].

In this Letter we show that the periodic flattening of the density and temperature profiles at mid-pedestal occur due to the onset of long-wavelength broadband fluctuation at the bottom of the Er-well. The same flattening at mid-pedestal is seen on multiple diagnostics at different toroidal and poloidal locations (CER, Thomson) and from I-coil reversal experiments, confirming the axisymmetry of the staircase structure. The fluctuations at mid-pedestal occur due to incomplete E×B suppression of long wavelength instabilities. The fluctuations do not destroy the H-mode barrier, and in-fact the pedestal width and pressure increase during periods of enhanced mid-pedestal fluctuations. This suggests that enhanced turbulence in the pedestal is not necessarily deleterious to confinement, so long as it is spatially localized, consistent with general arguments for the beneficial effect of wide pedestals on PBM stability [8]. Local gyrokinetic analysis using the CGYRO [9] code indicates a non-monotonic flux gradient relation at the mid-pedestal which can lead to a local transport bifurcation. The staircase pedestal occurs due to this transport bifurcation from KBM to trapped-electron-mode (TEM) limited transport. The pedestal transitions between these two states as the flux through the pedestal rises and falls with the penetration and screening of resonant fields at the pedestal top as described in Refs. [6, 10]. We note that staircase structures were first discovered in global gyrokinetic simulations [11] where quasi-coherent flow structures were generated by the underlying turbulence field, and more recently through avalanching [12], and inhomogeneous turbulent mixing [13]. The formation of staircase structures in the pedestal and its relation to E×B shear has not been described in the literature to date.

Figure 1a shows the Balmer (D_α) signal and n=3 RMP wave form for a discharge with suppressed large amplitude (Type-I) ELMs and showing only residual grassy-ELMs. A zoom in view of the modulations in heat flux

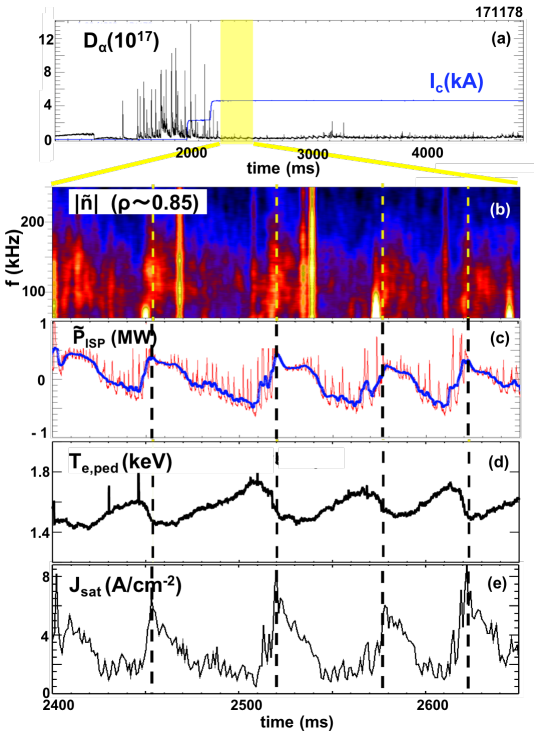

FIG. 1: (a) Balmer signal D_α from inner strike point and I-coil current (I_C), (b) BES density fluctuations at $\rho \approx 0.85$ (c) inner strike point heat flux $\tilde{P}_{\rm ISP}$(red) measured by IR camera and 2 ms average of heat flux in blue (d) pedestal top temperature from ECE (e) ion saturation current density at the inner strike point. Plasma parameters are $q95 \approx 5.3$, R ≈ 1.68 m, $a \approx 0.6$ m, $B_T \approx -1.90$ T, $Ip \approx 1.15$ MA, $P_{\rm NBI} \approx 10$ MW, $P_{\rm EC} \approx 3.4$ MW and ITER shape δ=0.55.

to the inner strike point (Fig. 1c, using an infra-red camera, with $\approx$ 2 MW subtracted) and fast measurements of the electron temperature at $\rho = 0.7$ (Fig. 1d, from ECE [14]) reveals pulsations correlated with broadband fluctuations at the top of the pedestal (Fig. 1b, from beam emission spectroscopy (BES) [15] measurements at $\rho \approx 0.85$, $\rho = \sqrt{\psi_N}$, ψ_N is the poloidal flux function normalized to its value on the last closed flux surface). A 2 ms time average of the IR signal in Fig. 1c (blue) shows the minimal contribution of grassy-ELMs to the time average heat flux. Langmuir probe measurements of ion saturation current at the inner strike point, shown in Fig. 1e, reveals increased particle flux to the divertor coincident with the increase in the heat flux. The slow modulation of the heat and particle flux to the divertor is correlated with the modulation in the fluctuation level at the top of the pedestal (Fig. 1b). Correlated with the observed enhancement in the pedestal-top fluctuations, the temperature at $\rho = 0.7$ shows rapid drops during periods of enhanced particle and heat flux to the divertor at the times indicated by the vertical dashed lines in Fig. 1.

Here we show that as the flux to the divertor rises and falls (Fig.1c,1e) the mid-pedestal undergoes a transport bifurcation from KBM/ETG to TEM limited transport, leading to pedestal broadening and staircase formation.

Figure 2 shows a close-up view of fluctuations and profiles between t=2460 to 2540 ms from Fig. 1. Broadband density fluctuations from BES measurements at the pedestal top ($\rho \approx 0.85$) and at the mid-pedestal ($\rho \approx 0.95$) are shown in Figs. 2a and 2b respectively. The 25% change in the heat flux to the inner strike point is shown in Figure 2c (red) together with a 3 ms average of the heat flux (blue). Here, the high frequency peaks in the heat flux are due to grassy-ELMs. The increase in the heat flux to the inner strike point is correlated with the increase in the amplitude of turbulent fluctuation at the top of the pedestal ($\rho \approx 0.85$). In contrast, the bursting broadband fluctuations (f$\approx$40-160 kHz) at the mid-pedestal ($\rho \approx 0.95$) occur during the period of decreasing heat flux to the divertor. These bursts have distinct temporal and spectral features to the and the grassy-ELMs, and have a poloidal velocity of $\approx$ 20 km/s moving in the electron diamagnetic direction in the lab frame (similar to the ExB velocity at the bottom of E_r well). Pedestal profiles are shown in Fig. 2(d-g). The blue profiles correspond to the period of decreasing heat flux to the divertor (blue shaded region in Fig. 2c), and the red profiles correspond to the period of increasing heat flux to the divertor (red shaded region in Fig. 2c). These profiles are obtained by ensemble averaging Thomson scattering (TS) and C-VI charge exchange measurements (CER) over 10 similar periods of these pedestal oscillation. The ion temperature profiles (not-shown) have a similar mid-pedestal flattening as with the electron temperature. The E×B rotation frequency $\omega_E = E_r/RB_p$ (Fig. 2g), and E×B shearing rate $\gamma_E = r/q\partial_r\omega_E$ [r, q minor radius and safety factor] (Fig. 3b) are obtained from radial force balance using the CER data.

During the interval of increasing heat and particle flux (red shaded region in Fig. 2c) the pedestal contracts to a single-step structure with a width $\Delta\rho \approx 0.08$ (compared to $\Delta\rho \approx 0.12$ for the staircase pedestal). The narrower pedestal has a typical Tanh shape that we call the *single-step* pedestal. During the interval of decreasing heat flux we observe a two-step structure that we call the *staircase* pedestal resulting from the strong flattening of profiles at mid-pedestal. The mid-pedestal profile flattening is correlated with the appearance of bursting fluctuation at the same location.

Linear instabilities We employ linear CGYRO to find the dominant modes, their growth rates, frequencies and quasilinear fluxes at different radial locations. CGYRO uses an advanced collision operator relevant for the edge of fusion plasmas. We use a toroidally symmetric general equilibrium that realistically models the plasma geometry, and we use the full physics available in CGYRO (fully electromagnetic, collisional, all species kinetic). Dominant instability types at different radii are summarized

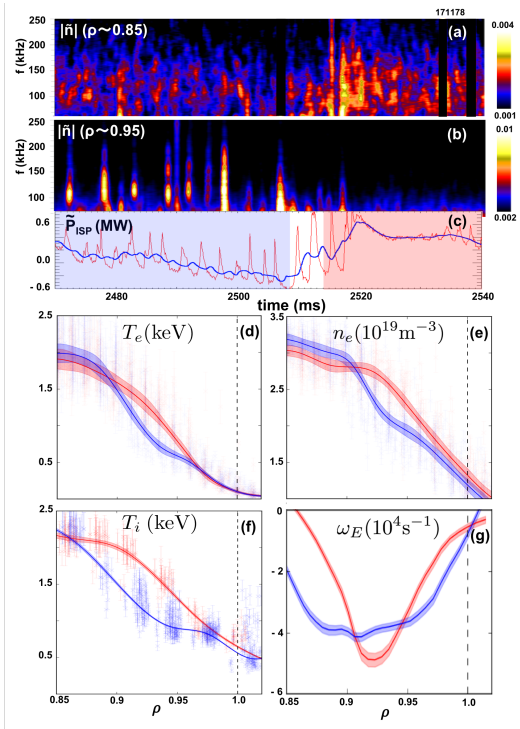

FIG. 2: Power spectrum of density fluctuation measured by BES at (a) pedestal top (b) mid-pedestal. (c) heat flux $\tilde{P}_{\rm ISP}$ at the inner strike point. Figures (d)-(g) are respectively, electron temperature, electron density, ion temperature, and E×B toroidal rotation frequency (ω_E).

ρ	Single-step	Staircase
0.85 (pedestal top)	MT ($k_\theta\rho_s < 0.1$) ITG ($0.1 < k_\theta\rho_s < 2$) ETG ($k_\theta\rho_s > 2$)	MT ($k_\theta\rho_s < 0.1$) ITG ($0.1 < k_\theta\rho_s < 2$) ETG ($k_\theta\rho_s > 2$)
0.9 (core-edge boundary)	TEM/ITG ($k_\theta\rho_s < 2$) ETG ($k_\theta\rho_s > 2$)	TEM/ITG ($k_\theta\rho_s < 2$) ETG ($k_\theta\rho_s > 2$)
0.95 (mid-pedestal)	TEM ($k_\theta\rho_s < 0.3$) ETG ($k_\theta\rho_s > 0.3$)	MT ($k_\theta\rho_s < 0.1$) TEM/ITG ($0.1 < k_\theta\rho_s < 2$) ETG ($k_\theta\rho_s > 2$)
0.98 (pedestal foot)	TEM ($k_\theta\rho_s < 0.3$) ETG ($k_\theta\rho_s > 0.3$)	TEM ($k_\theta\rho_s < 0.3$) ETG ($k_\theta\rho_s > 0.3$)

TABLE I: Table of instability types in the pedestal

in table I for the staircase and single-step pedestal. Identification of the dominant instabilities from CGYRO is based on the sign of the mode frequencies and their dependence on parameters such as $\beta_e, \nabla T_{e,i}, \nabla n$, and relative quasilinear fluxes. The linear simulations are performed for the ballooning angle $\theta_0 = 0$, assuming that the dominant instabilities are poloidally centered at the outboard midplane. For both pedestals, Ion Temperature Gradient modes (ITG) dominate at the pedestal top and Electron Temperature Gradient modes (ETG) dominate at the pedestal foot ($\rho = 0.98$).

At mid-pedestal ($\rho = 0.95$) in the single-step pedestal we find the linear growth rate of unstable TEM in the range $k_\theta\rho_s < 0.15$ is smaller than γ_E at the same location (k_θ is the binormal mode number [9]). However, ETG is unstable at mid-pedestal and the pressure gradient is within 10% of KBM threshold, so it is likely that a combination of ETG and KBM control the mid-pedestal transport. In contrast, for the staircase pedestal, unstable TEM and ITG are found in the range $0.1 < k_\theta\rho_s < 2$ and they have linear growth rates exceeding γ_E by an order of magnitude. Therefore we anticipate that TEM/ITG will dominate the mid-pedestal transport for the staircase pedestal. The dominant staircase mid-pedestal instabilities are similar to the pedestal top instabilities, since the gradients at mid-pedestal are similar to the pedestal top.

Nonlinear CGYRO simulations at $\rho = 0.95$ (including E×B shear) for the single-step pedestal shows that electron thermal transport is mostly driven by ETG, whereas residual TEMs at long-wavelengths ($k_\theta\rho_s \leq 0.15$) drive weak particle and ion thermal transport due to strong E×B shear suppression. For electron scales (32 toroidal modes, $3 \leq k_\theta\rho_s \leq 93$) ETGs dominate the transport through electron energy channel, and particle and ion thermal transport are negligible ($Q_e \approx Q_{\rm tot} = 223 Q_{\rm gB}$, $\Gamma_e = 0.38\Gamma_{\rm gB}$). For ion-scale simulations (32 toroidal modes, $k_\theta\rho_s \leq 1.55$) particle, ion energy, and electron energy transport are respectively, $\Gamma_e \approx 4\Gamma_{\rm gB}$, $Q_i = 50 Q_{\rm gB}$, $Q_e = 200 Q_{\rm gB}$. Neoclassical transport using the NEO code (NEO is a multi-species drift-kinetic solver) [16] at mid-pedestal shows negligible electron transport and significant ion heat transport ($Q_i = 57$ gB, $\Gamma_e \sim 0.85$ gB). The net thermal and particle flux from nonlinear CGYRO and NEO is $Q_{\rm tot} = 530 Q_{\rm gB}$, $\Gamma = 6\Gamma_{\rm gB}$, comparable to the net heat and particle flux obtained from TRANSP [17] transport code analysis, $Q_{\rm tot} = 460 Q_{\rm gB}$, $\Gamma = 5\Gamma_{\rm gB}$.

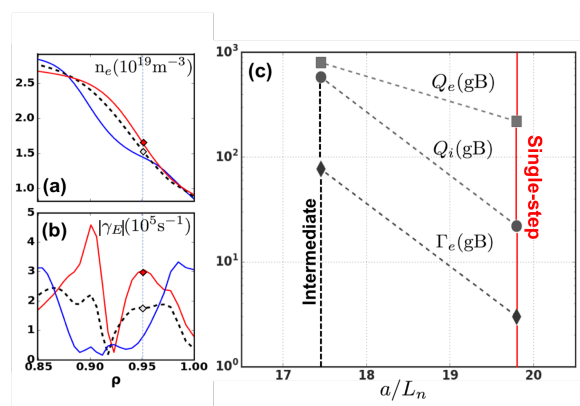

FIG. 3: Single-step and intermediate pedestal profiles and nonlinear flux calculations. (a) Electron density for single step (red) staircase blue and intermediate profile (dashed (b)E×B shearing rate for the single-step(red), staircase(blue) the intermediate (dashed) (c) Nonlinear fluxes from CGYRO of particle, electron energy and ion energy (Γ_e, Q_e, Q_i) in their respective gyro-Bohm units (gB), for the single-step pedestal (red) and the intermediate pedestal (black).

To better understand the sensitivity of the mid-pedestal transport on the E×B shear, we take the single-

step pedestal and make it broader by 20% and increase the pressure by 20% (10% increase in temperature and density). This creates an intermediate pedestal profile between the single-step and staircase profiles, as shown by the dashed curve in Fig. 3a. Figure 3b shows $\approx 40\%$ decrease in γ_E at $\rho = 0.95$ for the intermediate pedestal due to approximate quadratic dependence of γ_E on the pressure inverse scale-length.

For the intermediate pedestal, nonlinear ion-scale CGYRO simulations at $\rho = 0.95$ show a dramatic increase of fluxes in all channels (Q_e, Q_i and Γ_e) compared to single-step pedestal simulations, shown in Fig.3c. In particular the particle and ion thermal flux increase by more than an order of magnitude in going from the single-step to the intermediate profile, even though the profile gradients have been relaxed. A relaxation of the gradients should lead to a reduction in the turbulent flux but the strong reduction of the ExB shear enhances the long-wavelength TEM transport capable of driving large energy and particle flux at mid-pedestal.

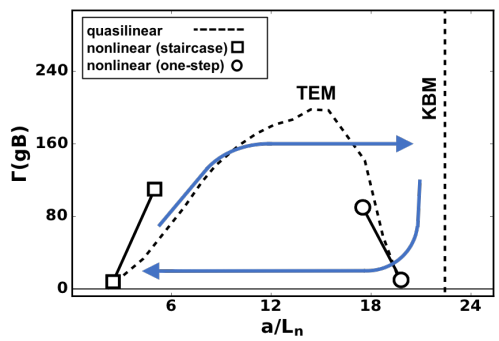

FIG. 4: Local particle flux versus a/L_n, squares and circle are the nonlinear fluxes, and dashed lines are from quasilinear calculation.

The negative slope of the flux versus inverse scale-length in Fig. 3c is a property of a nonlinearly unstable flux-gradient solution which can trigger a local transport bifurcation [18]. In a physical flux driven system, the profile gradient will immediately relax in response to an infinitesimal enhancement in transport when the flux-gradient solution is unstable, producing the staircase pedestal consistent with a transport bifurcation.

Once the mid-pedestal undergoes a transport bifurcation to the weak gradient state, the flux versus gradient relation becomes positive (stable solution). Figure 4 shows a a non-monotonic flux gradient relation calculated using linear and non-linear CGYRO that demonstrates how flux-driven transitions can occur from the staircase to the single-step pedestal and visa versa. From nonlinear ion-scale CGYRO simulations at $\rho = 0.95$, doubling the gradients for the staircase pedestal leads to a large increase in fluxes as shown by square open symbols in Fig. 4 consistent with a stable flux-gradient relation. The open circles in Fig. 4 show the flux versus inverse scale length for the single-step and the intermediate pedestal profiles obtained from nonlinear CGYRO, presented in Fig. 3c. The negative slope demonstrates an unstable flux gradient relation. The KBM critical gradient is shown by the vertical dashed line in Fig. 4, which is within 10% of the measured gradient at mid-pedestal.

To connect these two regions in the flux-gradient relation we use a quasilinear calculation (dashed curve) derived by scanning the scale lengths (a/L_n and a/L_T) at $\rho = 0.95$ in the single-step pedestal and calculate the linear growth rate and quasilinear flux for each scale length. In this scan the ratio of density and temperature scale lengths are kept constant. The quasilinear mixing length estimate for the effective particle diffusivity is $D = D_0(1 - \gamma_E/\gamma)$, where $D_0 = c\gamma/k_\perp^2$ [19], c is a coefficient for matching the flux to the nonlinear simulation, $k_\perp = [k_\theta^2(1 + \hat{s}^2 \langle\theta^2\rangle)]^{0.5}$ is the perpendicular wave number, $\hat{s} = r/q\partial_r q$ is the magnetic shear, and θ is the extended ballooning angle representing the distance along the magnetic field line. The mixing-length particle flux is given by $\Gamma = -\max[D]\nabla \mathrm{n}$ [20], and the value of γ_E is self-consistently calculated with the density scale length. The quasilinear flux qualitatively captures the stable and unstable trends in the flux-gradient relation obtained by nonlinear simulations.

The transport bifurcation dynamics can now be elucidated from the left pointing and right pointing blue arrows in Fig. 4. Starting from the staircase pedestal at $a/L_n = 2.5$ (lower left), an increase in the flux through the pedestal will drive an increase in the gradients, producing the trajectory of the upward right pointing blue arrow. This is the phase when the transport at the mid-pedestal is dominated by ITG/TEM. As the gradient increases beyond a critical threshold [18] the profile bifurcates to the KMB limit indicated by the horizontal part of the right pointing arrow. This bifurcation corresponds to the E×B shear suppression of ITG/TEM transport. Conversely, as the flux decreases, the trajectory follows the left pointing arrow. Initially the gradients relax from the KBM to the unstable flux-gradient region. This leads to a bifurcation of the profile from the single-step to the staircase pedestal as indicated by the blue left pointing arrow. This bifurcation corresponds to enhanced TEM transport at mid-pedestal as the E×B shear relaxes. The cycle repeats so long as there is a significant modulation in the thermal and particle transport through the pedestal, which is correlated with the modulation of the turbulence at the top of pedestal (Fig. 1b) and flux to the divertor (Fig. 1c,1e).

In this work we show that a wide pedestal can experience a transport bifurcation to a staircase structure when the E×B shear is insufficient to fully suppress long wave-length electrostatic instabilities. Modulated fluxes of particles and energy through the pedestal drives transitions between a staircase structure limited by ITG/TEM

at the mid-pedestal to a single-step structure limited by ETG/KBM. The strong flattening in the mid-pedestal region is correlated with bursting broadband fluctuations. Taking the ExB rotation (ω_E) at the bottom of the Er-well and the nonlinear spectrum from CGYRO at $\rho = 0.95$, we obtain a frequency range of 50-140 kHz in the electron diamagnetic direction in the lab frame, which is comparable to the BES bursting fluctuation spectrum. As noted in this Letter, the E×B shearing rate decreases rapidly with increasing pedestal width, creating the conditions where pedestal transport bifurcations can occur. In ITER, ρ^* will be about an order of magnitude smaller than in DIII-D and the pedestal width is expected to scale with the machine size. As $\gamma_E/\gamma \sim \rho^*$ (γ is the dominant mode growth rate) [19], we anticipate that suppression of TEM/ITG modes will not be as effective in ITER as in current devices, leading to the possible formation of a staircase pedestal as seen in DIII-D. The consequences of enhanced ITG/TEM in the ITER pedestal are not necessarily deleterious as the pedestal pressure increases in DIII-D in the staircase phase. Therefore the consequence of staircase pedestal formation in ITER or future reactors could be beneficial for confinement.

This material is based upon work supported by the U.S. Department of Energy, Office of Science, Office of Fusion Energy Sciences, using the DIII-D National Fusion Facility, a DOE Office of Science user facility, under Awards DE-FC02-04ER54698 and DE-AC02-09CH11466

DISCLAIMER

This report was prepared as an account of work sponsored by an agency of the United States Government. Neither the United States Government nor any agency thereof, nor any of their employees, makes any warranty, express or implied, or assumes any legal liability or responsibility for the accuracy, completeness, or usefulness of any information, apparatus, product, or process disclosed, or represents that its use would not infringe privately owned rights. Reference herein to any specific commercial product, process, or service by trade name, trademark, manufacturer, or otherwise, does not necessarily constitute or imply its endorsement, recommendation, or favoring by the United States Government or any agency thereof. The views and opinions of authors expressed herein do not necessarily state or reflect those of the United States Government or any agency thereof.

[1] F. Wagner, G. Fussmann, T. Grave, M. Keilhacker, M. Kornherr, K. Lackner, K. McCormick, E. R. Muller, A. Stabler, G. Becker, K. Bernhardi, U. Ditte, Eberhagen, O. Gehre, J. Gernhardt, G. V. Gierke, E. Glock, O. Gruber, G. Haas, M. Hesse, G. Janeschitz, F. Karger, S. Kissel, O. Kluber, G. Lisitano, H. M. Mayer, D. Meisel, V. Mertens, H. Murmann, W. Poschenrieder, H. Rapp, H. Rohr, F. Ryter, F. Schneider, G. Siller, P. Smeulders, F. Soldner, E. Speth, K. H. Steuer, Z. Szymanski, and O. Vollmer, Phys. Rev. Lett. **53**, 1453 (1984).

[2] K. H. Burrell, Plasma Phys. Controlled Fusion **36**, A291 (1994).

[3] P. Snyder, R. Groebner, J. Hughes, T. Osborne, M. Beurskens, A. Leonard, H. Wilson, and X. Xu, Nucl. Fusion **51**, 103016 (2011).

[4] M. Kotschenreuther, D. Hatch, S. Mahajan, P. Valanju, L. Zheng, and X. Liu, Nucl. Fusion **57**, 064001 (2017).

[5] D. Hatch, D.Told, F. Jenko, H. Doerk, M. Dunne, E. Wolfrum, E. Viezzer, The ASDEX Upgrade Team3, and M. Pueschel, Nucl. Fusion **55**, 063028 (2015).

[6] R. Nazikian, C. Petty, A. Bortolon, X. Chen, D. Eldon, T. Evans, B. Grierson, N. Ferarro, S. Haskey, M. Knolker, C. Lasnier, N. Logan, R. Moyer, D. Orlov, T. Osborne, C. Paz-Soldan, F. Turco, H. Wang, and D. Weisberg, Nucl. Fusion **58**, 106010 (31pp) (2018).

[7] G. L. Jackson, P. A. Politzer, D. A. Humphreys, T. A. Casper, A. W. Hyatt, J. A. Leuer, J. Lohr, T. C. Luce, M. A. V. Zeeland, and J. H. Yu, Phys. Plasmas **17**, 056116 (2005).

[8] T. Osborne, G. Jackson, Z. Yan, R. Maingi, D. Mansfield, B. Grierson, C. Chrobak, A. McLean, S. Allen, D. Battaglia, A. Briesemeister, M. Fenstermacher, G. McKee, P. Snyder, and The DIII-D Team, Nucl. Fusion **55**, 063028 (2015).

[9] J. Candy, E. Belli, and R. Bravenec, J. Comp. Phys. **324**, 73 (2016).

[10] R. Fitzpatrick, Phys. Plasmas **25**, 112505 (2018).

[11] G. Dif-Pradalier, P. H. Diamond, V. Grandgirard, Y. Sarazin, J. Abiteboul, X. Garbet, P. Ghendrih, A. Strugarek, S. Ku, and C. S. Chang, Phys. Rev. E **82**, 025401(R) (2010).

[12] Y. Kosuga, P. H. Diamond, G. Dif-Pradalier, and Ö. D. Gürcan, Phys. of Plasmas **21**, 055701 (2014).

[13] A. Ashourvan and P. H. Diamond, Phys Rev. E **94**, 051202(R) (2016).

[14] M. Austin and J. Lohr, Rev. Sci. Instrum. **74**, 1457 (2003).

[15] G. McKee, R. Ashley, R. Durst, R. Fonck, M. Jakubowski, K. Tritz, K. Burrell, C. Greenfield, and J. Robinson, Rev. Sci. Instrum. **70**, 913 (1999).

[16] E. Belli and J. Candy, Plasma Phys. Control. Fusion **50**, 095010 (2008).

[17] F. Poli, J. Sachdev, J. Breslau, M. Gorelenkova, and X. Yuan, "Transp v18.2," [Computer Software] `https://dx.doi.org/10.11578/dc.20180627.4` (2018).

[18] V. Lebedev and P. H. Diamond, Phys. Plasmas **4**, 1087 (1997).

[19] R. E. Waltz, G. D. Kerbel, J. Milovich, and G. W. Hammett, Phys. Plasmas **1**, 2229 (1994).

[20] F. Jenko, T. Dannert, and C. Angioni, Plasma Phys. Controlled Fusion **47**, B195 (2005).